

Medical image denoising comparison between c-BM3D, Non-local mean filter and autoencoders.

Tan Sy NGUYEN

August 22, 2021

1 Motivation

The gastric burden is increasing with the fact of growing population and due to the formation of cancer in the gastrointestinal tract (GI) around the world. Every year nearly 0.7 million cases of specifically gastric cancer are reported (ACS [1]). It is estimated that cancer cases in both sexes are **11,180 deaths are estimated in 2021 and 26,560 new cases in the United States alone**. The normal clinical practice includes the intestinal biopsy (tissues sample of the mucosa is taken) of GI tract. Which are then analyzed by experts (under microscope), to see if there are any cancerous or abnormal cells exist. This is an invasive method for detection of gastric abnormalities and it requires high-level of expertise. On the other hand, endoscopy is a less invasive method for screening GI tract (Kainuma et al. [2]). An endoscope is a flexible tube with a mounted camera, light source, and an accessory channel (Pennazio [3]). Moreover, an accessory channel can be used for cleansing of GI tract or inserting medical instruments. Therefore, the endoscope can also be used for the intestinal biopsy (Wallace and Keisslich [4]).

The GI tract can be categorized into several parts, starting from upper stomach parts GI tract have esophagus, stomach in middle, and duodenum as ending of stomach (upper GI tract), the jejunum, ileum (small-bowel), ending at the colon, and rectum (Carpi et al. [5]; Filip et al. [6]). Therefore, the endoscopy procedures refer to different names according to the target area of GI tract e.g., for esophagus referred (esophagoscopy), area of stomach and duodenum (gastroscopy), rectum and sigmoid colon (proctoscopy), sigmoid colon (sigmoidoscopy), colon (colonoscopy) for whole GI tract (laparoscopy).

The endoscopic procedure helps the physician for the detection of gastric abnormalities in their early stages. Timely detection of chronic diseases can be cured with proper treatments. Thus, the screening process can be very useful for a substantial reduction in both, death-rate as well as the cost of treatment. Specifically, the deaths occur due to different gastrointestinal cancers, which can be cured if cancer was detected in its pre-malignant stage (Hamashima et al. [7]). Still, video endoscopy is a painful procedure, it also requires both time and expertise.

In contrast with the wired endoscopy, the wireless capsule endoscopy (WCE) is a painless tool than traditionally used white light video endoscopy (VE) for examining the internal cavity of the human body (Gastelum et al. [8]; Kim et al. [9]). Normally, a VE composed of a light source, a charged couple camera (CCD), and a video monitor (which is used to view the output of the endoscope).

1.1 Abnormalities in gastrointestinal tract

The GI tract is a crucial part of human body, it refers to stomach, small intestine and whole digestive system. The GI tract can be divided into an esophagus, stomach, small bowel and colon (Chu et al. [10]). Furthermore, the stomach has its own parts as the upper stomach, middle stomach and lower stomach (Miyahara et al. [11]). A brief introduction of the parts of a GI tract has given in Table 1.

Table 1: Anatomy of the gastrointestinal tract

Disease	Description
Esophagus	When we eat food, the chewed food goes into the esophagus. The esophagus is a tube-like organ that used to carry food to the stomach (Khashab et al. [12]). The entry point of food into the stomach is called gastroesophageal (GE) junction, which is located under the lungs (Owens and Appelman [13])
Stomach	The stomach is a towel-like organ that holds food (Eberlein et al. [14]). After the food arrived from esophageal the special enzymes are produced to digest the food into that stomach (Roukos et al. [15])
Small-bowel	Secretion of stomach juices and the food are mixed. Then, the food goes into the entrance of small-intestine called duodenum (Callacondo-Riva et al. [16]). The small-intestine is like a narrow tube of approximately 6 meters in length. Due to complexity and length of small intestine, the screening is a difficult and time-consuming task (Axon [17])
Colon	The last portion of GI tract, and the most prone area for having tumors and polyps. The colon cancer is the third most common disease found in the Western countries (Chu et al. [10]). The colon is consisting of several parts, ascending colon, transverse colon, descending colon and rectum (Hurlstone et al. [18])

There are many clinical conditions, including basic symptoms and mature diseases found in the GI tract. Some of these abnormalities of the digestive system are listed below. Moreover, some of them can be easily detected through a normal endoscopic procedure. However, there are some diseases in GI tract (e.g., cancer, polyps and ulcers) that do not exhibit visible signs until it approaches an advance stage (Liedlgruber and Supervisor [19]).

1. Cancer: There are many types of cancer [e.g., adenocarcinoma (Guggenheim [20]), lymphoma (Namikawa et al. [21]), GIST (Korngold [22]), etc.]. However, most of

the cancers are started from an unusual growth of cells. The older cells do not die and unusual growth of cells forms cancer. Some common symptoms of gastric cancer include early satiety, abdominal pain, nausea, vomiting, bloating, weight-loss, and anorexia (Rogy and Bünger [23]). It is worth mentioning here, that cancer can start in any area of the GI tract.

2. Polyps: Polyps are similar to cancer, it is also an unusual mucosal growth and typically these are benign (Kato et al. [24]). On the other hand, there could be diminutive colorectal polyps, which are very dangerous if left untreated. Polyps can grow in any area of GI tract similar to cancer. However, it is mostly found in the colon and small-bowel (Hazewinkel et al. [25]).
3. Ulcer: The ulcer is also referred to a disease caused by the acid that is produced by the stomach itself. In peptic ulcer, the gastric cells are damaged with gastric juices. Normally ulcer appears in the duodenum, small intestine or in gastric lining (Jensen et al. [26]).
4. Crohn's Disease: Crohn's disease is caused due to inflammation of the lining of the gut. This is an intestinal inflammatory disease, it may also cause a severe abdominal pain. In some cases ileum (part of small intestine) is affected from this disease (Eliakim [27]).
5. Bleeding: Bleeding is another abnormality that is normally found in GI tract while screening. It may be caused by different other pathological conditions such as cancer, Crohn's disease or ulcer (Schlag et al. [28]).
6. Angiodysplasia: Angiodysplasia is an abnormality with the blood vessels in the gastrointestinal (GI) tract. The GI tract includes the mouth, esophagus, small and large intestines, stomach, and anus. This condition causes swollen or enlarged blood vessels, as well as the formation of bleeding lesions in the colon and stomach (Sotiropoulou [29]).

1.2 Distortions in WCE

Today, medical endoscopy is a widely used procedure to inspect the inner cavities of the human body. As a consequence different medical fields exist for which automated decision-support systems based on endoscopic images have been developed [19]. But since images taken with endoscopes often suffer from various kinds of degradations, a pre-processing of the images is often necessary in order to make them useful for an automated analysis [30] (to cope with e.g. sensor noise, focus and motion blur, and specular reflections [19]).

In [31] the impact of distortion correction on the classification accuracy regarding celiac disease images has been investigated. Gschwandtner et al. showed that applying barrel distortion correction as a pre-processing step to the endoscopic images is a absolutely important stage to increase the classification accuracy. However, to the best of our knowledge up to now there are only a few studies available, which investigate the impact of various distortions and distortion correction on the accuracy of automated classification systems for endoscopic

images. Many papers focus on a mono-distortion and propose a certain pre-processing stage for all images while there are many kinds of distortion [21, 24, 26] which can occur in one observed test case [32, 33, 34].

Therefore, in order to improve performance of existing pre-processing stage, image quality assessment (IQA) metrics is an unavoidable tool. However, with the quick advancement of IQA research, the booming of open IQA databases calls for associated comprehensive and accurate visual attention dataset. Table 3 gives an overview of some existing datasets of images and videos for IQA.

Table 3: IQA dataset

Dataset	Description
IVC	database consists of 10 pristine images, and 235 distorted images, including four types of distortions (JPEG, JPEG2000, locally adaptive resolution coding, blurring). Quality score ratings (1 to 5) are provided in the form of MOS.
LIVE IQA	has two releases, Release 1 and Release 2. Laboratory for Image and Video Engineering (University of Texas at Austin) conducted an extensive experiment to obtain scores from human subjects for a number of images distorted with different distortion types. Release 2 has more distortion types—JPEG (169 images), JPEG2000 (175 images), Gaussian blur (145 images), White noise (145 images), bit errors in JPEG2000 bit stream (145 images). The subjective quality scores in this database are DMOS (DifferentialMOS), ranging from 0 to 100.
A57 Database	has 3 pristine images, and 54 distorted images, including six types of distortions due to coding by JPEG, JPEG2000, JPEG2000 with dynamic contrast-based quantization, quantization of the LH subbands of DWT, additive Gaussian white noise, Gaussian blurring. Quality score ratings (0 to 1) are provided in the form of DMOS
Toyoma Database	consists of 14 pristine images, and 168 distorted images, including two types of distortions (JPEG, JPEG2000). Quality score ratings (1 to 5) are provided in the form of MOS.
TID2008	contains 25 reference images and 1,700 distorted images (25 reference images x 17 types of distortions x 4 levels of distortions images. The MOS was obtained from the results of 838 experiments carried out by observers from three countries. 838 observers have performed 256,428 comparisons of visual quality of distorted images or 512,856 evaluations of relative visual quality in image pairs. Higher value of MOS (0 - minimal, 9 - maximal, MSE of each score is 0.019) corresponds to higher visual quality of the image. A file enclosed “mos.txt” contains the Mean Opinion Score for each distorted image.

CSIQ	database consists of 30 original images, each distorted using one of six types of distortions, each at four to five different levels of distortion. The distortions used in CSIQ are: JPEG compression, JPEG-2000 compression, global contrast decrements, additive pink Gaussian noise, and Gaussian blurring. The images were subjectively rated based on a linear displacement of the images across four calibrated monitors placed side-by-side with equal viewing distance to the observer. The database contains 5,000 subjective ratings from 35 different subjects.
IVC-LAR	database contains 8 pristine images (4 natural images and 4 art images), and 120 distorted images, consisting of three types of distortions (JPEG, JPEG2000, locally adaptive resolution coding). Quality score ratings (1 to 5) are provided in the form of MOS.
IRSQ	consists of 57 reference images grouped into four attributes, specifically face and people, clear foreground object, natural scenery, and geometric structure. Moreover, ten different retargeting methods (cropping, seam carving, scaling, shift-map editing, scale and stretch, etc.) are applied to generate retargeted images. In total, 171 test images can be found in this database.
TID2013	contains 25 reference images and 3,000 distorted images (25 reference images x 24 types of distortions x 5 levels of distortions). MOS (Mean Opinion Score) is provided as subjective score, ranging from 0 to 9.
KADID-10k	consists of 81 pristine images and 10, 125 distorted images derived from the pristine images considering 25 different distortion types at 5 intensity levels (10, 125 = 81x25x5). In contrast, KADIS-700k contains 140, 000 pristine images and distorted images were derived using 25 different distortion types at 5 intensity levels but MOS values are not given in this database.
CID2013	database contains 474 images with authentic distortions captured by 79 imaging devices, such as mobile phones, digital still cameras, and digital single-lens reflex cameras.

However, deep learning methods for classification are infamous for being data hungry. For problems in natural image analysis, this is often solved by mining massive numbers photos from social media and having non-experts perform annotations through crowdsourcing. For medical problems, this data is often harder to acquire and labeling requires expensive experts, meaning it takes longer for deep learning methods to find their way to medical image analysis. As a result, many of the algorithms for classification are prototyped on natural data and subsequently adjusted to medical problems. We can clearly see that those mentioned IQA datasets are natural image which challenge the real-life endoscopic imaging classification task. Therefore, our motivation is creating a new endoscopic dataset which contains different level of different types of distortion.

2 Hyper-Kvair dataset

Endoscopy is currently the gold-standard procedure for examining the GI tract, but its effectiveness is considerably limited by the variation in operator performance. The recent rise of artificial intelligence (AI)-enabled support systems has shown promise in giving healthcare professionals the tools needed to provide quality care at a large scale. The core of an efficient AI-based system is the combination of quality data and algorithms which teach a model to solve real-world problems like detecting pre-cancerous lesions or cancers in images. However, health data is often sparse and hard to obtain due to legal constraints and structural problems in data collection. Nevertheless, an increasing number of promising AI solutions aimed for diagnostics in endoscopy are being developed. The datasets used for these systems, like CVC [35, 36] and the ASU-Mayo polyp database [37], are rather small in the context of ML research. Hyper-Kvasir dataset is the most new and complete dataset which can deal with the data-hurry of ML problem. Table 4 shows some existing dataset for GI image processing

2.1 Overview

In total, HyperKvasir contains 110,079 images (10,662 labeled and 99,417 unlabeled images) from the GI tract. In total, the dataset contains 10,662 labeled images stored using the JPEG format of 23 different classes. Fig. 1 shows us the number of images belonging to each class. Details about image resolutions can be found in the Figs. 2 and the categories of the labeled image can be found in Fig. 3. The size of the labeled images is presented in the Fig. 4

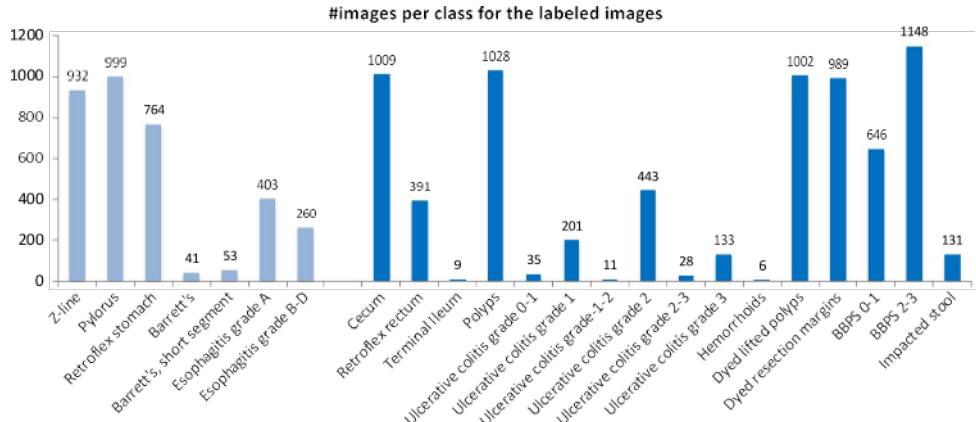


Figure 1: The number of images in the various HyperKvasir labeled image classes according to the file folders

From this analysis (Fig. 4), we can decide the main size of image to be processed is approximately (600, 550)

These classes are structured according to location in the GI tract and the type of finding. They defined four main categories of findings where the first and the third are found both in the upper and lower GI tract:

- **Anatomical landmarks:** Anatomical landmarks are characteristics of the GI tract used for orientation during endoscopic procedures. Furthermore, they are used to

Table 4: An overview of existing GI datasets.

Dataset	Findings	Size
CVC-356 [35]	Polyps	356 images
CVC-ClinicDB (also named CVC-612) [36]	Polyps	612 images
CVC-VideoClinicDB (also named CVC-12k) [35]	Polyps	11954 images
CVC-ColonDB [35]	Polyps	380 images
Endoscopy Artifact detection 2019 [38]	Endoscopic Artifacts	5,138 images
ASU-Mayo polyp database [37]	Polyps	18,781 images
ETIS-Larib Polyp DB [39]	Polyps	196 images
KID [40]	Angiectasia, bleeding, inflammations, polyps	2371 images and 47 videos
GIANA 2017 [41]	Polyps & Angiodysplasia	3462 images and 38 videos
GIANA 2018 [42]	Polyps & Small bowel lesions	8262 images and 38 videos
GASTROLAB [43]	GI lesions	Some 100s of images and few videos
WEO Clinical Endoscopy Atlas [44]	GI lesions	152 images
GI Lesions in Regular Colonoscopy Data Set [45]	GI lesions	76 images
Atlas of Gastrointestinal Endoscope [46]	GI lesions	1295 images
El salvador atlas of gastrointestinal video endoscopy [47]	GI lesions	5071 video clips
Kvasir [48]	Polyps, esophagitis, ulcerative colitis, Z-line,pylorus cecum, dyed polyp, dyed resection margins, stool	8000 images
Kvasir-SEG [49]	Polyps	1000 images
Nerthus [50]	Stool - categorization of bowel cleanliness	21 videos

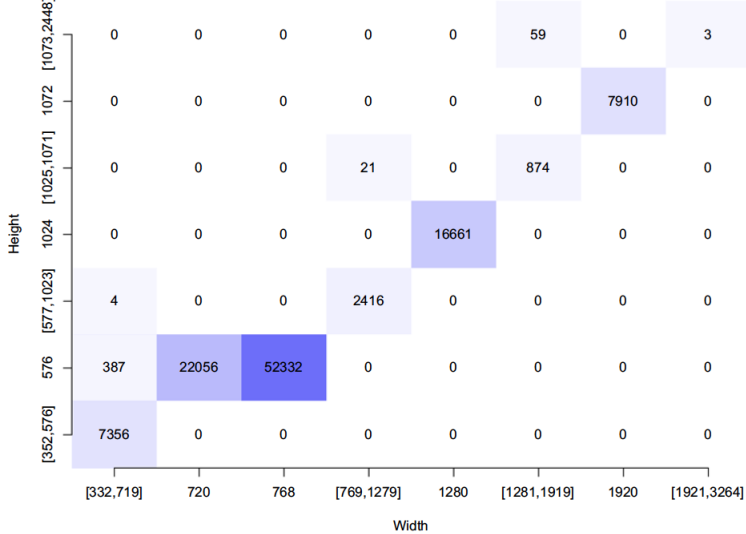


Figure 2: Resolution of the 110,079 images in HyperKvasir

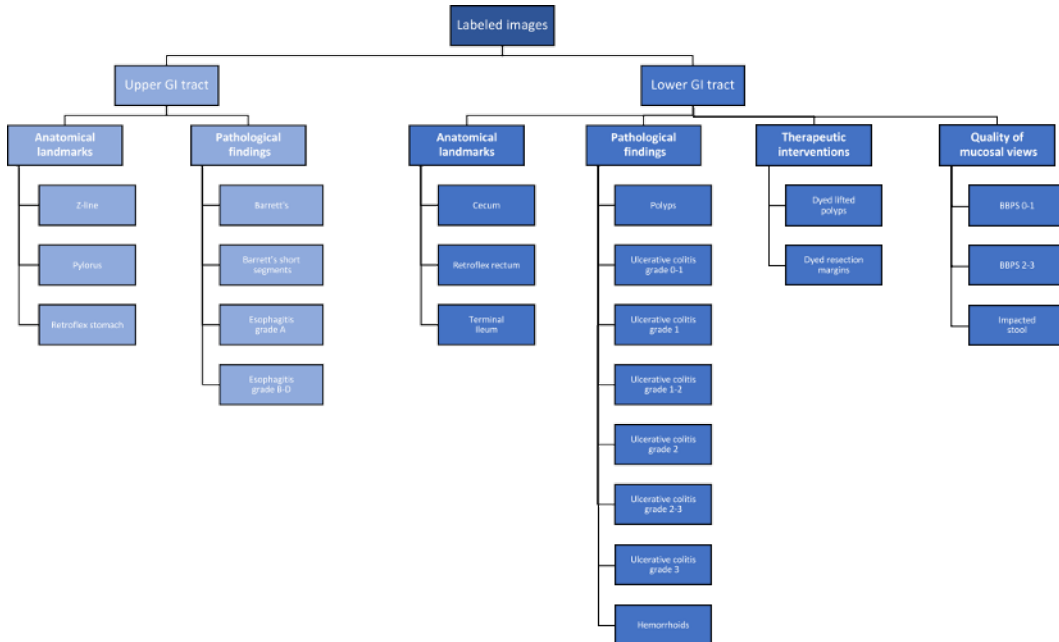


Figure 3: The various image classes structured under position and type, also the structure of the stored images

confirm a complete extent of the examination. Landmarks exist both in the upper GI tract (esophagus, stomach and duodenum) and in the lower GI tract (terminal ileum, colon and rectum). However, in the small bowel, there are no specific landmarks to be used for topographical localization of a lesion.

- **Quality of mucosal views:** Complete visualization of all the mucosa is crucial not to overlook pathological findings. In the colon, there exist a classification for the quality of the mucosal visualisation, the Boston Bowel Preparation Scale (BBPS).

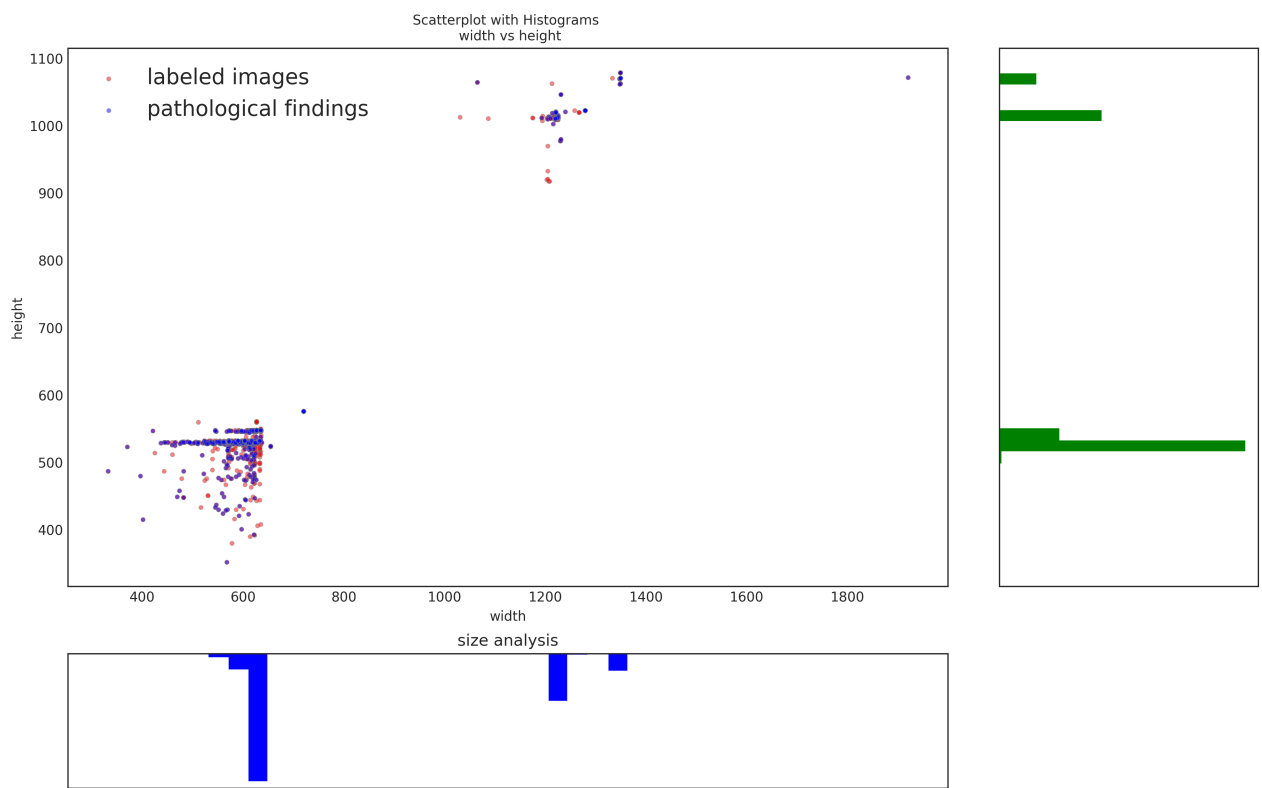


Figure 4: Size histogram of 10k labeled images in general and 2742 pathological findings images in particular

- **Pathological findings:** All parts of the gastrointestinal tract can be affected by abnormalities or findings due to disease. Most pathological findings can be seen as more or less obvious changes in the intestinal wall mucosa. These findings are classified according to the Minimal Standard Terminology, defined by the World Endoscopy Organization
- **Therapeutic interventions:** When a lesion or pathological finding is detected, a therapeutic intervention is frequently required to treat the condition, e.g., limiting and resecting a polyp, dilation of a stenosis or injection of a bleeding ulcer.

2.2 Additive white Gaussian noise (AWGN)

The various type noises affecting various types of images are Gaussian Noise, Poisson Noise, Impulse Noise and Quantization noise. While manifestation of any type of noise in various images is an entirely random stochastic process, the Additive White Gaussian Noise is the most prevalent noise in images as it occurs during acquisition and transmission through analogy circuitry which is pretty much the basic operation required for computerised operation [51].

Additive white Gaussian noise (AWGN) is a basic noise model used in information theory to mimic the effect of many random processes that occur in nature. Digital imaging is widely used in applications such as medical, biometrics, multimedia,...etc. In many cases, images are transmitted through Internet from one point to another. During image acquisition and transmission, factors such as moving objects, sensor quality, and channel interferences may result in additive noise. Parameters such as noise mean and variance provide noise characteristics of AWGN.

In the last decade, classical noise suppression methods, including the use of bilateral filters and Gaussian blur filters, may produce erroneous and unusual CE results [52]. The ability to reduce noise while maintaining the details of images is required for CE. Non-local means filters, adaptive median (AM) filters, block-matching and 3D filtering, and K-nearest neighbor filters have been compared in terms of their endoscopy-image correcting abilities. The AM filter, particularly, showed better results in reducing impulse noise while preserving image details than other 3 methods. Gopi et al. [53] have proposed double density dual-tree complex wavelet transform (DDDT-CWT) methods for reducing noise of images. These authors first converted images into YCbCr color spaces. They then applied a DDDT-CWT-based grayscale noise reduction method separately for each color spaces. They demonstrated the performance of DDDT-CWT by comparing the DDDT-CWT method to three other methods.

2.2.1 AWGN model

Image independent noise can often be described by an additive noise model, where the recorded image $f(i, j)$ is the sum of the true image $s(i, j)$ and the noise $n(i, j)$:

$$f(i, j) = s(i, j) + n(i, j) \quad (1)$$

The noise $n(i, j)$ is often zero-mean and described by its variance σ_n^2 . The impact of the noise on the image is often described by the signal to noise ratio (SNR), which is given by:

$$SNR = \frac{\sigma_s}{\sigma_n} = \sqrt{\frac{\sigma_f^2}{\sigma_n^2} - 1} \quad (2)$$

where σ_s^2 and σ_f^2 are the variances of the true image and the recorded image, respectively. The image after being applied AWGN noise will be clipped to maintain the proper image data range. Therefore, the output will be on the range $[0, 1]$.

2.2.2 Study of noise in HyperKvasir dataset

HyperKvasir dataset has a existing AWGN which requires us to know. the estimation of Noise will be the important pre-step to process the denosing stage. Follow that requirement, I have chosen the fast noise variance estimator with threshold [54]. In this method, the standard deviation of additive white Gaussian noise in an image is estimated using a noise estimation mask. This suggested mask, M_N has been generated using a difference of two 3×3 masks, each approximating the Laplacian of an image. For an image I with width W and height H , the estimated standard deviation σ_n of noise is estimated as:

$$\sigma_n = \sqrt{\frac{\pi}{2}} \frac{1}{6(W-2)(H-2)} \sum_{x,y} |I(x, y) * M_N| \quad (3)$$

where $M_N = 2(L_2 - L_1)$ with the given L_1, L_2 :

$$L_1 = \begin{bmatrix} 0 & 1 & 0 \\ 1 & -4 & 1 \\ 0 & 1 & 0 \end{bmatrix} \quad (4)$$

$$L_2 = \begin{bmatrix} 1 & 0 & 1 \\ 0 & -4 & 0 \\ 1 & 0 & 1 \end{bmatrix} \quad (5)$$

Based on above equation, I have constructed an experiment to analyze the existing AWGN in labeled image as well as pathological finding images in particular. The result is shown in Fig. 5

From the histogram, we can see that the main noise standard deviation in HyperKvasir labeled images is 0.35. Therefore, I will choose the value set of $\sigma_n = [0.25, 0.3, 0.35, 0.4, 0.6, 0.65, 0.7]$ to test the denoising method in the following section.

3 Study of denoising methods

Image denoising, being a classical problem in computer vision has been studied in detail. Various methods exist, ranging from models based on partial differential equations (PDEs)

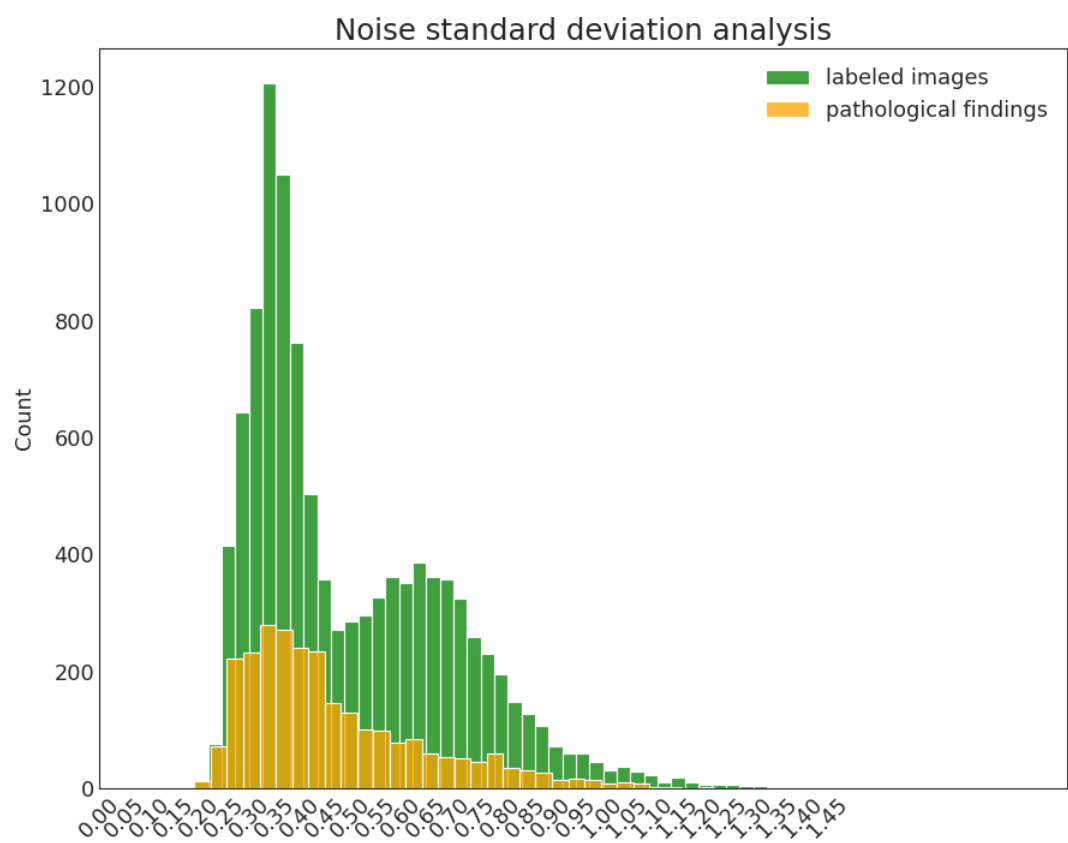


Figure 5: Noise estimation histogram of 10k labeled images in general and 2742 pathological findings images in particular

[55, 56, 57], domain transformations such as wavelets [58], DCT [59], etc., non local techniques including NL-means [60], combination of non local means and domain transformations such as BM3D [61, 62]. All methods share a common goal, expressed as:

$$f = s + n \quad (6)$$

Where z is the noisy image produced as a sum of original image s and some noise n . Most methods try to approximate s using f as close as possible. In most cases, n is assumed to be generated from a well defined process.

With recent developments in deep learning [63, 64, 65], results from models based on deep architectures have been promising. Autoencoders have been used for image denoising [66, 67, 68]. They easily outperform conventional denoising methods and are less restrictive for specification of noise generative processes. Denoising autoencoders constructed using convolutional layers have better image denoising performance for their ability to exploit strong spatial correlations.

Although BM3D [61] is considered state-of-the-art in image denoising and is a very well engineered method, Burger et al. [69] showed that a plain multi layer perceptron (MLP) can achieve similar denoising performance.

Denoising autoencoders are a recent addition to image denoising literature. Used as a building block for deep networks, they were introduced by Vincent et al. [66] as an extension to classic autoencoders. It was shown that denoising autoencoders can be stacked [67] to form a deep network by feeding the output of one denoising autoencoder to the one below it. Xie et al. [68] used stacked sparse autoencoders for image denoising and inpainting, it performed at par with KSVD.

3.1 Non-local Mean filtering

Non-local means [60] is an algorithm in image processing for image denoising. Unlike "local mean" filters, which take the mean value of a group of pixels surrounding a target pixel to smooth the image, non-local means filtering takes a mean of all pixels in the image, weighted by how similar these pixels are to the target pixel. This results in much greater post-filtering clarity, and less loss of detail in the image compared with local mean algorithms [59].

Suppose Ω is the area of an image, p and q are two points within the image. Then, the algorithm is:

$$u(p) = \frac{1}{C(p)} \int_{\Omega} v(q) \omega(p, q) dq \quad (7)$$

where $u(p)$ is the filtered value of the image at point p , $v(q)$ is the unfiltered value of the image at point q , $\omega(p, q)$ is the weighting function, and the integral is evaluated $\forall q \in \Omega$

$C(p)$ is a normalizing factor, given by:

$$C(p) = \int_{\Omega} \omega(p, q) dq. \quad (8)$$

The purpose of the weighting function, $\omega(p, q)$, is to determine how closely related the image at the point p is to the image at the point q . It can take many forms. The Gaussian

weighting function sets up a normal distribution with a mean, $\mu = B(p)$ and a variable standard deviation.

$$\omega(p, q) = e^{-\frac{|B(q) - B(p)|^2}{h^2}} \quad (9)$$

where h is the filtering parameter (i.e., standard deviation) and $B(p)$ is the local mean value of the image point values surrounding p . From rule of thumb, I set $h = \lceil 6\sigma_n \rceil$

where $B(p)$ is given by:

$$B(p) = \frac{1}{|R(p)|} \sum_{i \in R(p)} v(i) \quad (10)$$

where $R(p) \subseteq \Omega$ and is a square region of pixels surrounding p and $|R(p)|$ is the number of pixels in the region R .

3.2 C-BM3D for color images

In [62], Dabov et. al have introduced the BM3D for color image. They consider a noisy RGB image f_{rgb} modeled as $f_{rgb} = s_{rgb} + n_{rgb}$, where $s_{rgb} = [s_R, s_G, s_B]$ is the true image and $n_{rgb} = [n_R, n_G, n_B]$ is independent Gaussian noise, where $n_C \sim N(0, \sigma_c^2)$, for $C = R, G, B$. The flowchart is shown in Fig. 6

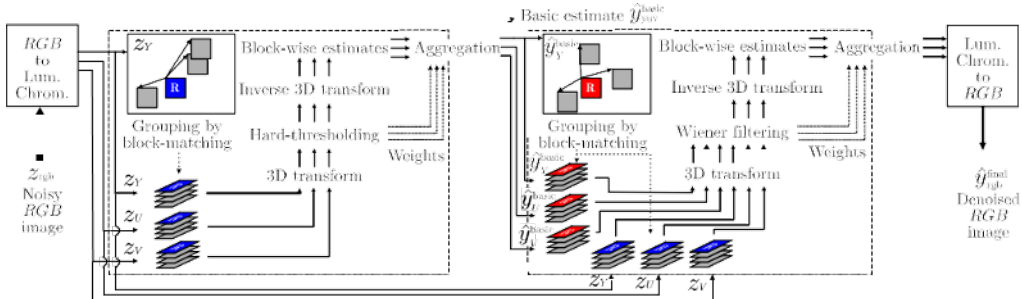


Figure 6: C-BM3D flowchart

3.3 Denoising Autoencoder

Denoising autoencoder is a stochastic extension to classic autoencoder [66], that is we force the model to learn reconstruction of input given its noisy version. A stochastic corruption process randomly sets some of the inputs to zero, forcing denoising autoencoder to predict missing(corrupted) values for randomly selected subsets of missing patterns.

Basic architecture of a denoising autoencoder is shown in Fig. 7 Denoising autoencoders can be stacked to create a deep network (stacked denoising autoencoder)[67]

3.3.1 Convolutional Autoencoder

Convolutional autoencoders are based on standard autoencoder architecture with convolutional encoding and decoding layers. Compared to classic autoencoders, convolutional autoencoders are better suited for image processing as they utilize full capability of convolutional neural networks to exploit image structure.

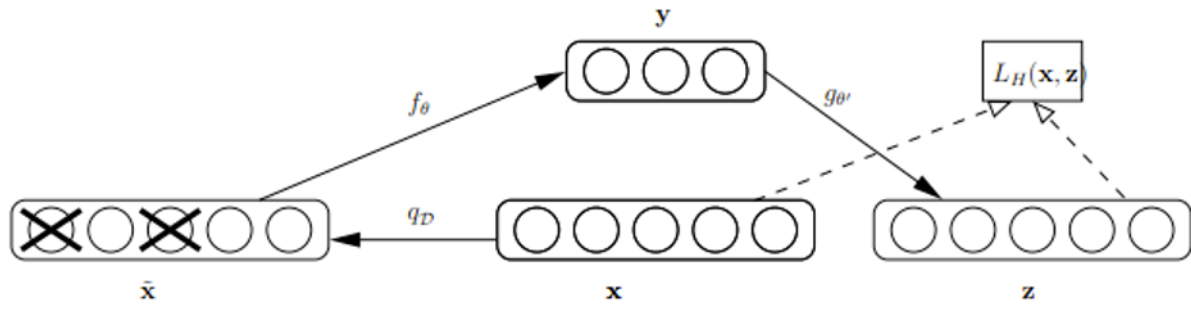


Figure 7: Basic architecture of a denoising autoencoder

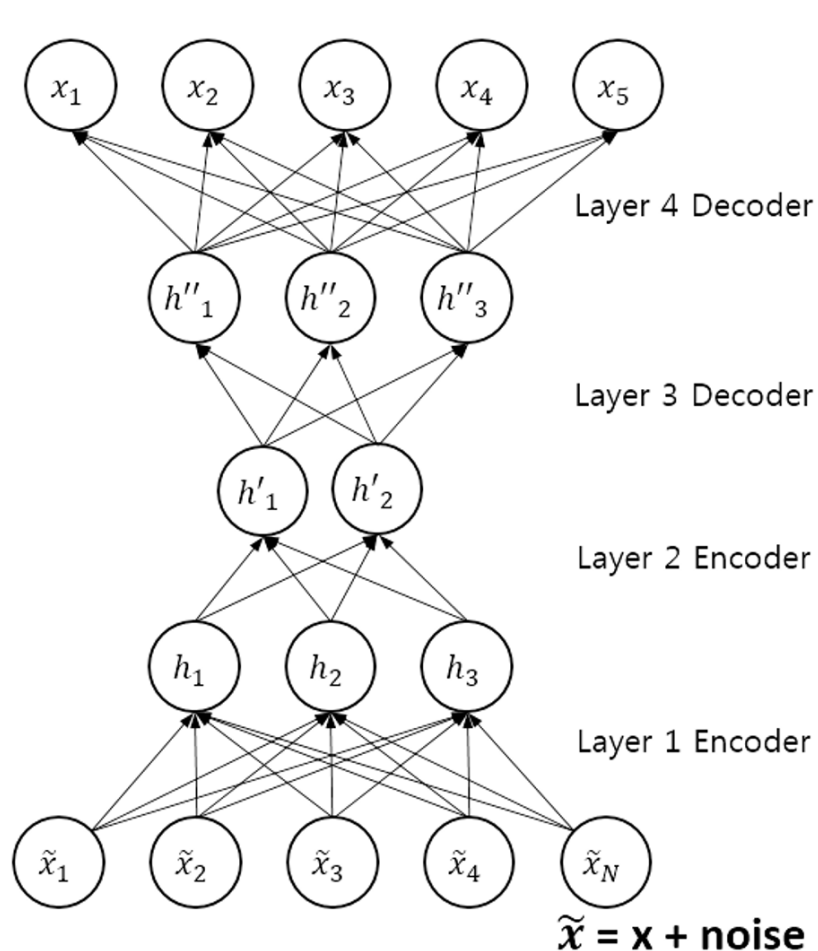


Figure 8: stacked denoising autoencoder archiecture

In convolutional autoencoders, weights are shared among all input locations which helps preserve local spatiality. Representation of i th feature map is given as

$$h^i = s(x * W^i + b^i) : \quad (11)$$

where bias is broadcasted to whole map, $*$ denotes convolution (2D) and s is an activation. Single bias per latent map is used and reconstruction is obtained as

$$y = s \sum_{i \in H} h^i * W^i + c \quad (12)$$

where c is bias per input channel, H is group of latent feature maps, W is flip operation over both weight dimensions. Back-propogation is used for computation of gradient of the error function with respect to the parameters.

4 Evaluation

4.1 Data

I used a subset of HyperKvasir dataset. This subset is the labeled images of pathological findings. It has 2742 images having the resolution which is shown in Fig. 4. The training and testing size proportion for autoencoder is 0.8 and 0.2, respectively. The considered size of images is 256×256 . The testing set is used to test the C-BM3D method [62] and ML-Mean method [60].

Table 5: Data setup

	C-BM3D		NL-Mean		CAE	
	Training set	Testing set	Training set	Testing set	Training set	Testing set
#sample	0	529	0	529	2113	529

4.2 Experimental Setting

Relatively simple architecture was used for convolutional denoising autoencoder (CAE), shown in Fig. 9. Keras was used for implementing this model on (Intel Core i7-super, 8 GB RAM, GPU RTX-2060 super). Images were compared using structural similarity index measure(SSIM) and peak signal to noise ratio (PSNR). Adam Optimizer with learning rate 0.1 was chosen for training in 50 epochs. A composite index of three measures, SSIM estimates the visual effects of shifts in image luminance, contrast and other remaining errors, collectively called structural changes. For original and coded signals x and y , SSIM is given as

$$SSIM(x; y) = [l(x; y)]^\alpha [c(x; y)]^\beta [s(x; y)]^\gamma \quad (13)$$

where α ; β and $\gamma > 0$ control the relative significance of each of three terms in SSIM and l , c and s are luminance, contrast and structural components calculated as

$$l(x; y) = \frac{2\mu_x\mu_y + C_1}{\mu_x^2 + \mu_y^2 + C_1} \quad (14)$$

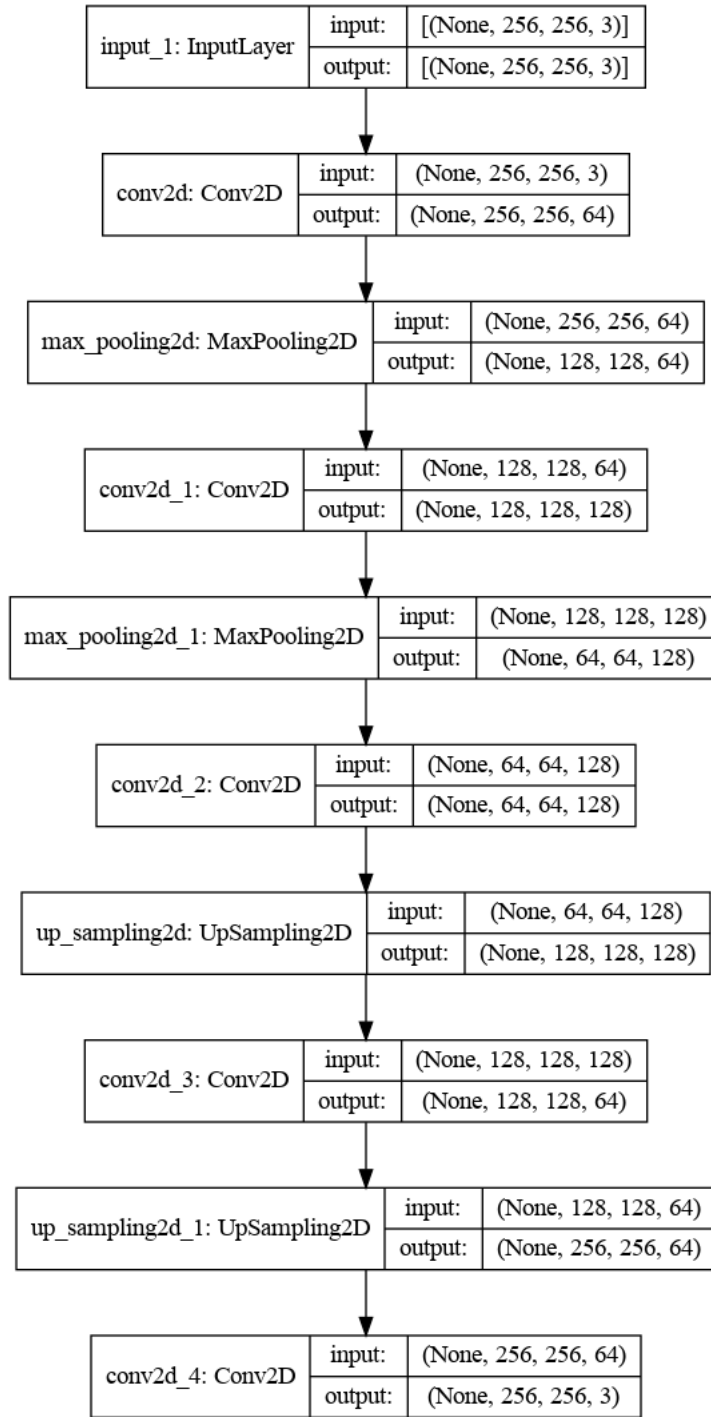


Figure 9: Used AE architecture

$$c(x; y) = \frac{2\sigma_x\sigma_y + C_2}{\sigma_x^2 + \sigma_y^2 + C_2} \quad (15)$$

$$s(x; y) = \frac{2\mu_{xy} + C_3}{\mu_x\mu_y + C_3} \quad (16)$$

where μ_x and μ_y represents the mean of original and coded image, σ_x and σ_y are standard deviation and σ_{xy} is the covariance of two images.

$$MSE = (1/(m * n)) * \sum(\sum((s - g).^2)) \quad (17)$$

$$PSNR = 20 * \log(\max(\max(s))) / ((MSE)^0.5) \quad (18)$$

where m, n is the width and height of the images. g and s is the denoised and original image, respectively.

4.3 Results

We assume that $f = s + n$ where n is the added AWGN, s is the original image. Table 6, Table 7 shows comparison of CAE with CBM3D and NL means for denoising performance on varying noise levels. It is clear that CAE outperforms both denoising methods by a wide margin, which increases as noise level increases.

Table 6: Comparison using mean SSIM for different level where $n \sim N(0, \sigma_n^2)$

	σ_n						
	0.25	0.3	0.35	0.4	0.6	0.65	0.7
Noisy-image	0.8095	0.7561	0.7084	0.6615	0.5102	0.4810	0.4508
C-BM3D	0.7364	0.7275	0.7106	0.7039	0.6517	0.6428	0.6389
NM-Mean	0.9068	0.8884	0.8752	0.8614	0.8222	0.8132	0.8051
CAE	0.9158	0.9097	0.9033	0.8991	0.8766	0.8681	0.8661

Table 7: Comparison using mean PSNR for different level where $n \sim N(0, \sigma_n^2)$

	σ_n						
	0.25	0.3	0.35	0.4	0.6	0.65	0.7
Noisy-image	32.89	31.44	30.34	29.32	26.37	25.85	25.22
C-BM3D	27.51	27.52	27.47	27.47	27.28	27.21	27.16
NM-Mean	35.81	34.74	34.12	33.48	31.85	31.51	31.14
CAE	32.28	32.56	32.70	32.38	31.42	31.18	31.43

It can be seen that as noise level increases, this simple network has trouble reconstructing original signal. However, even when the image is not visible to human eye, this network is successful in partial generation of real images. Using a more complex deeper model, or by increasing number of training samples and number of epochs might help.

The real images reconstructions are shown in Fig. 10, 11, 12, ??, 14, ??, 16 Besides

Medical Image Denoiser

Noise Proportion: 0.1 - Mean: 0 - Standard Deviation: 0.25

SSIM Results-> Noisy: 0.8095413961951142 - Denoised: 0.9158664033754269 - BM3D: 0.7364109365067012 - NL Means: 0.9068834745042688
PSNR Results-> Noisy: 32.89726123319729 - Denoised: 32.287927138645465 - BM3D: 27.510140712483718 - NL Means: 35.81046083975823

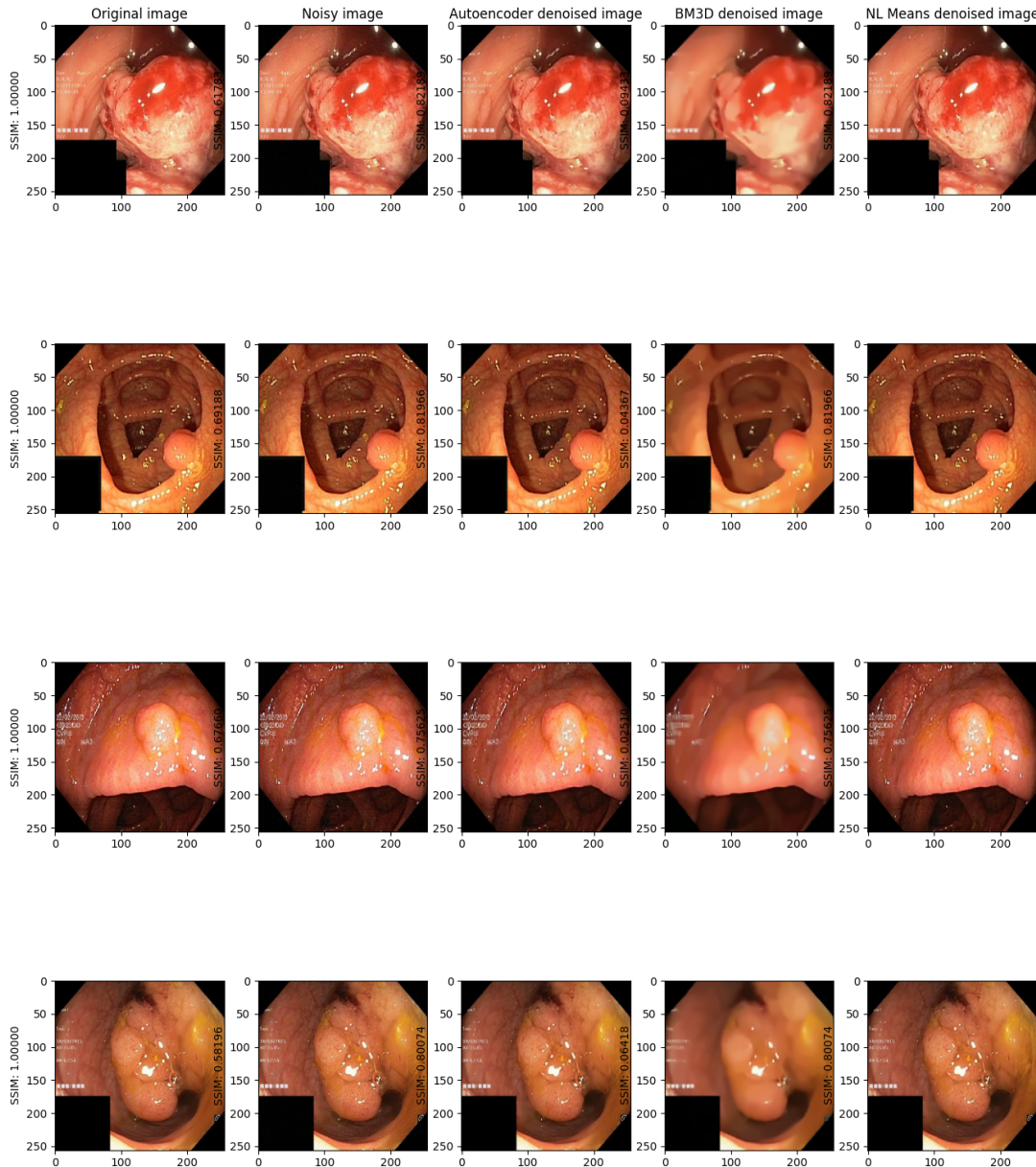


Figure 10: Denoising performance of CAE on different Gaussian noise patterns. Left column shows original images, second column is noisy images with noise levels of $\mu_n = 0$; $\sigma_n = 0.25$; third to fifth row shows denoising results

Medical Image Denoiser

Noise Proportion: 0.1 - Mean: 0 - Standard Deviation: 0.3

SSIM Results-> Noisy: 0.7561445663419875 - Denoised: 0.9097374711692165 - BM3D: 0.7275620971376207 - NL Means: 0.8884076968335964
PSNR Results-> Noisy: 31.446252512279372 - Denoised: 32.563280174930526 - BM3D: 27.520560336015315 - NL Means: 34.74850851285784

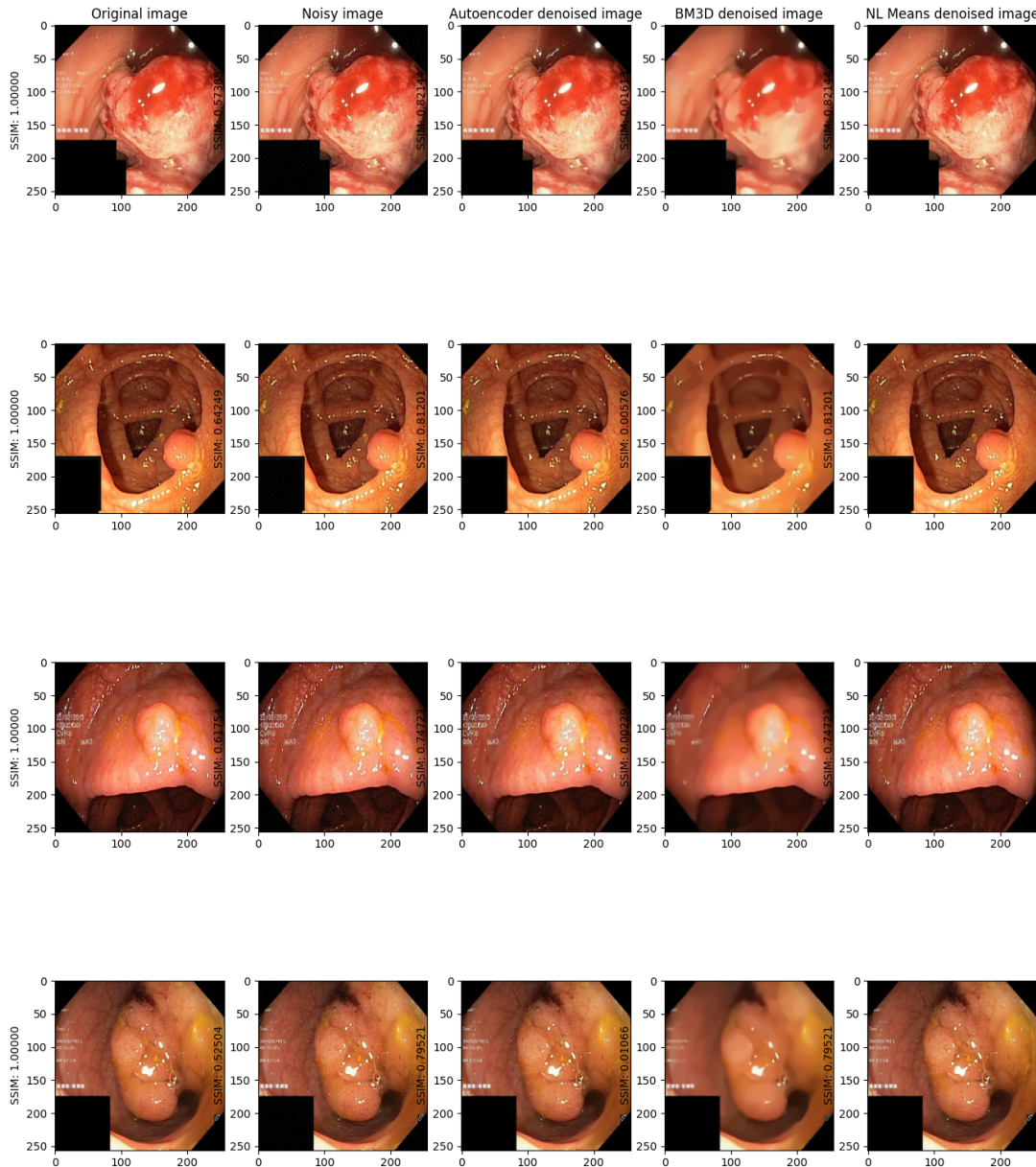


Figure 11: Denoising performance of CAE on different Gaussian noise patterns. Left column shows original images, second column is noisy images with noise levels of $\mu_n = 0$; $\sigma_n = 0.3$; third to fifth row shows denoising results

Medical Image Denoiser

Noise Proportion: 0.1 - Mean: 0 - Standard Deviation: 0.35

SSIM Results-> Noisy: 0.7084774750941896 - Denoised: 0.9033688606714723 - BM3D: 0.7106247735438498 - NL Means: 0.8752413640048642
PSNR Results-> Noisy: 30.344995321790265 - Denoised: 32.70924894452862 - BM3D: 27.47996903148159 - NL Means: 34.129033350418794

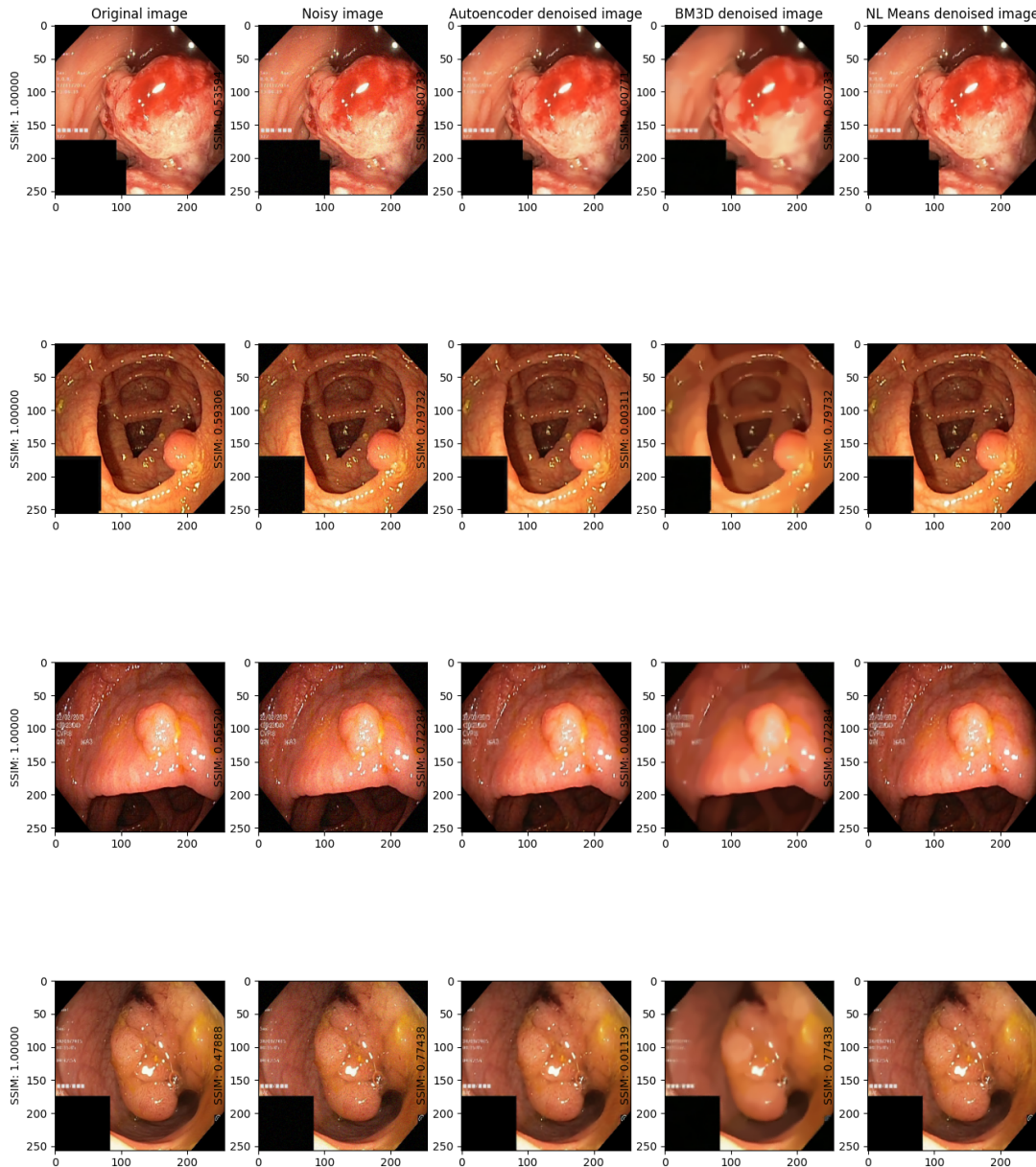


Figure 12: Denoising performance of CAE on different Gaussian noise patterns. Left column shows original images, second column is noisy images with noise levels of $\mu_n = 0$; $\sigma_n = 0.35$; third to fifth row shows denoising results

Medical Image Denoiser

Noise Proportion: 0.1 - Mean: 0 - Standard Deviation: 0.4

SSIM Results-> Noisy: 0.6615292634578471 - Denoised: 0.8991527193664816 - BM3D: 0.7038883531752462 - NL Means: 0.8614483624398745
PSNR Results-> Noisy: 29.32669731569964 - Denoised: 32.3801253191411 - BM3D: 27.473471132805482 - NL Means: 33.4857394112849

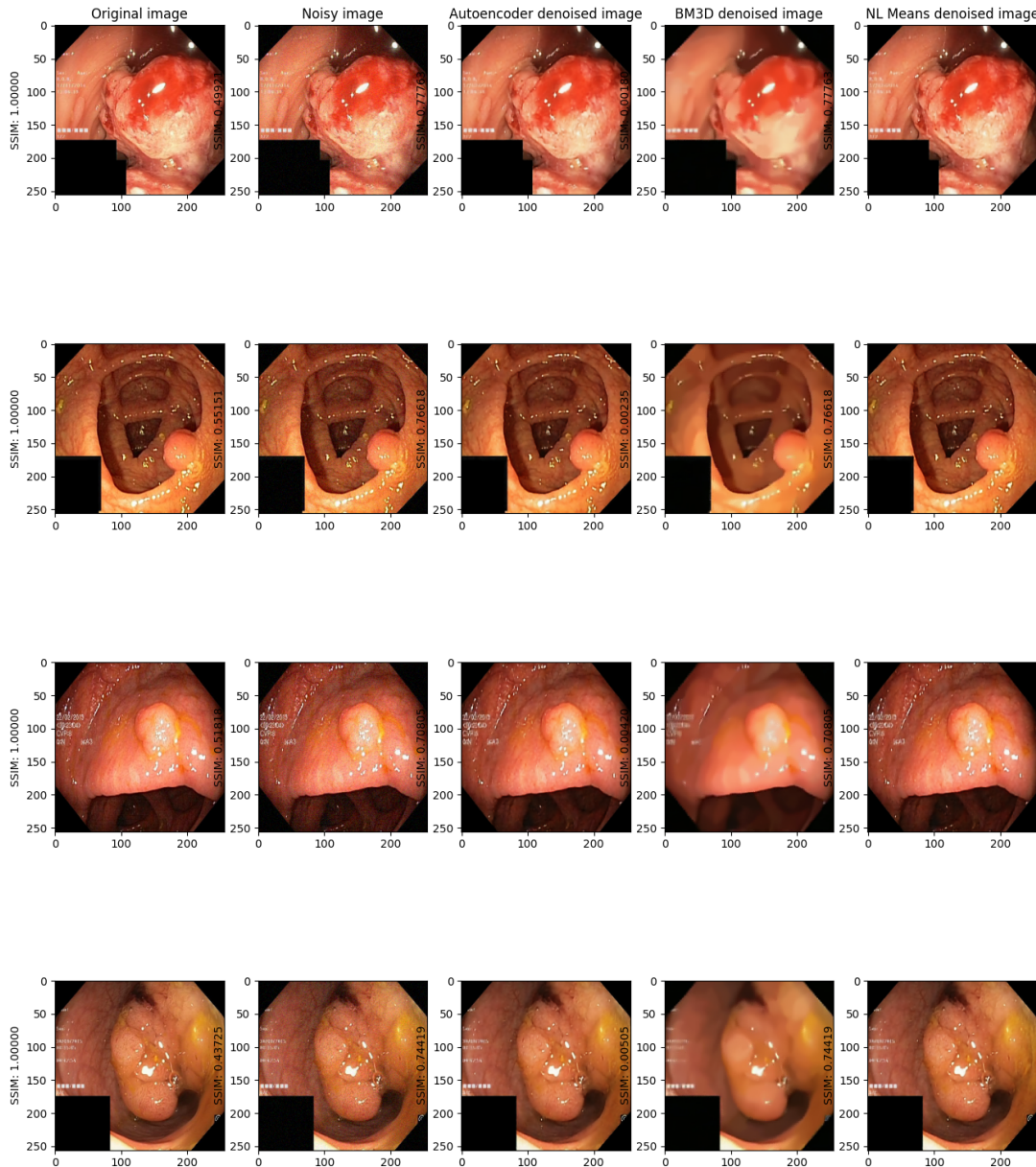


Figure 13: Denoising performance of CAE on different Gaussian noise patterns. Left column shows original images, second column is noisy images with noise levels of $\mu_n = 0$; $\sigma_n = 0.4$; third to fifth row shows denoising results

Medical Image Denoiser

Noise Proportion: 0.1 - Mean: 0 - Standard Deviation: 0.6

SSIM Results-> Noisy: 0.5102560169647559 - Denoised: 0.8766906242900697 - BM3D: 0.6517860884991861 - NL Means: 0.822292666514098
PSNR Results-> Noisy: 26.37113746315761 - Denoised: 31.42799819372732 - BM3D: 27.286495219190606 - NL Means: 31.85131052982325

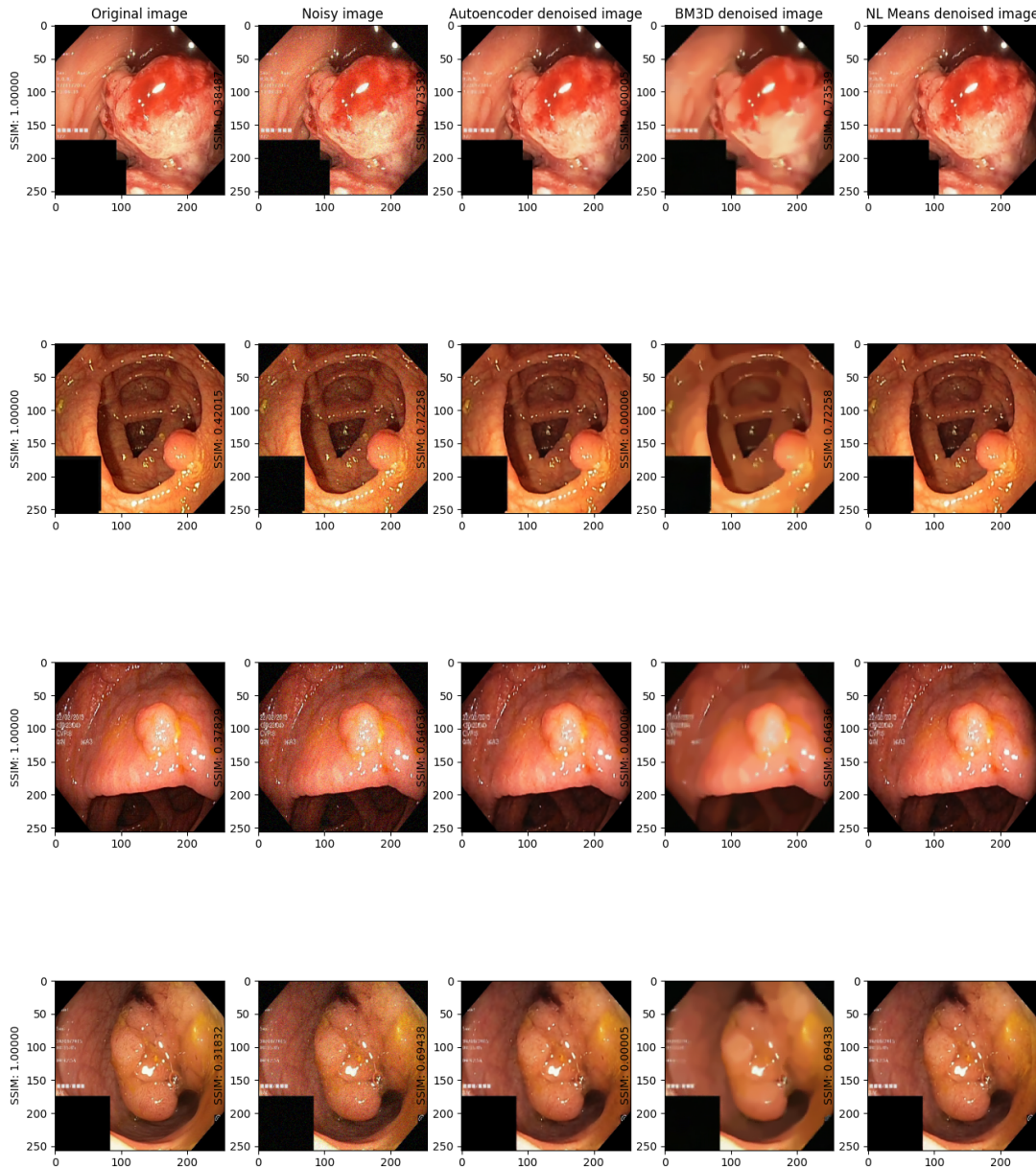


Figure 14: Denoising performance of CAE on different Gaussian noise patterns. Left column shows original images, second column is noisy images with noise levels of $\mu_n = 0$; $\sigma_n = 0.6$; third to fifth row shows denoising results

Medical Image Denoiser

Noise Proportion: 0.1 - Mean: 0 - Standard Deviation: 0.65

SSIM Results-> Noisy: 0.48099918036522227 - Denoised: 0.8681047561669865 - BM3D: 0.6428723463451683 - NL Means: 0.8132339883263666
PSNR Results-> Noisy: 25.85147848563596 - Denoised: 31.185528133616003 - BM3D: 27.21752554400395 - NL Means: 31.515235168958966

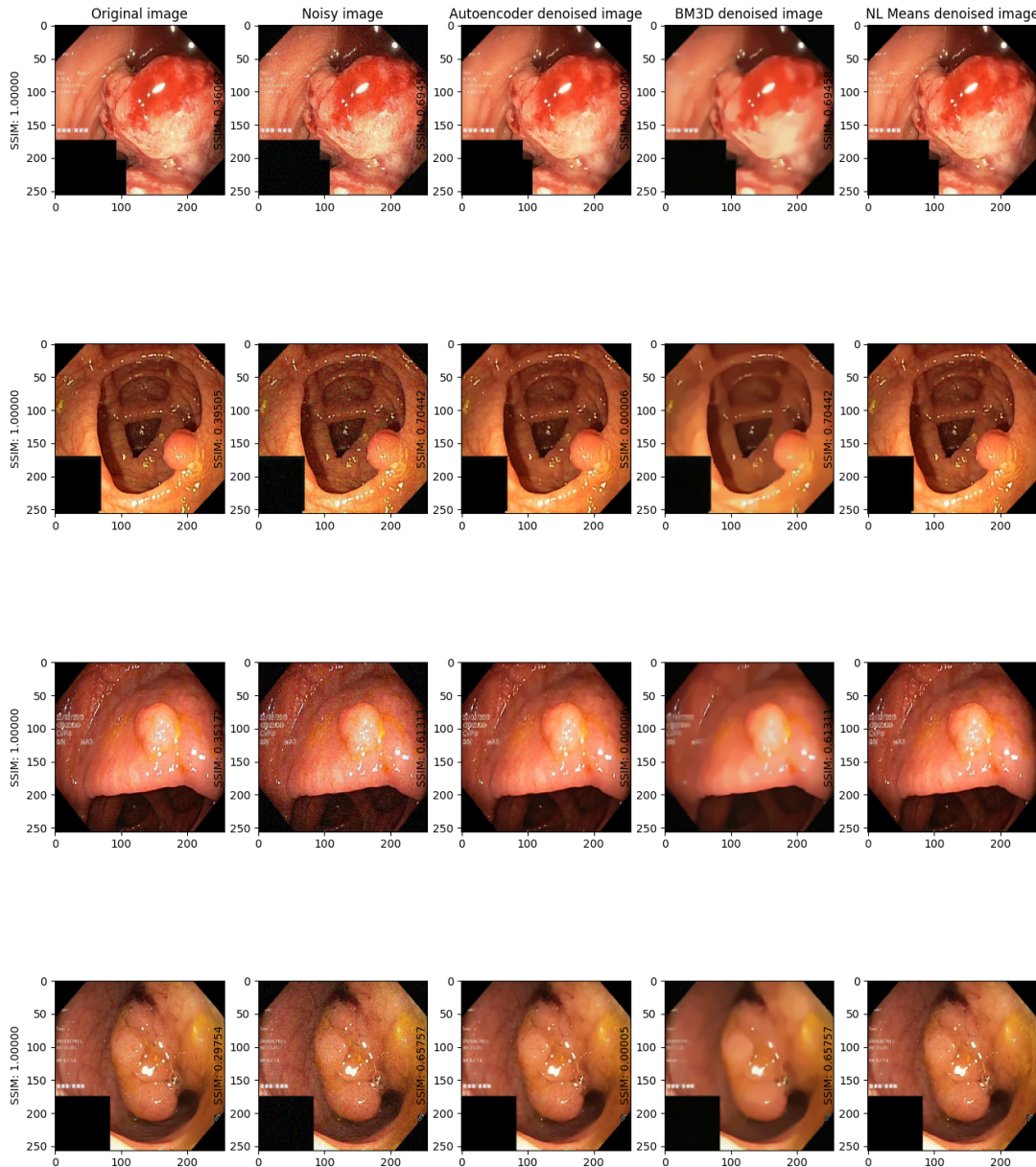


Figure 15: Denoising performance of CAE on different Gaussian noise patterns. Left column shows original images, second column is noisy images with noise levels of $\mu_n = 0$; $\sigma_n = 0.65$; third to fifth row shows denoising results

Medical Image Denoiser

Noise Proportion: 0.1 - Mean: 0 - Standard Deviation: 0.7

SSIM Results-> Noisy: 0.45081513601643575 - Denoised: 0.8661543788948016 - BM3D: 0.6389403145681385 - NL Means: 0.8051977049393415
PSNR Results-> Noisy: 25.22317465841487 - Denoised: 31.436120712323046 - BM3D: 27.164624923098735 - NL Means: 31.148274717789402

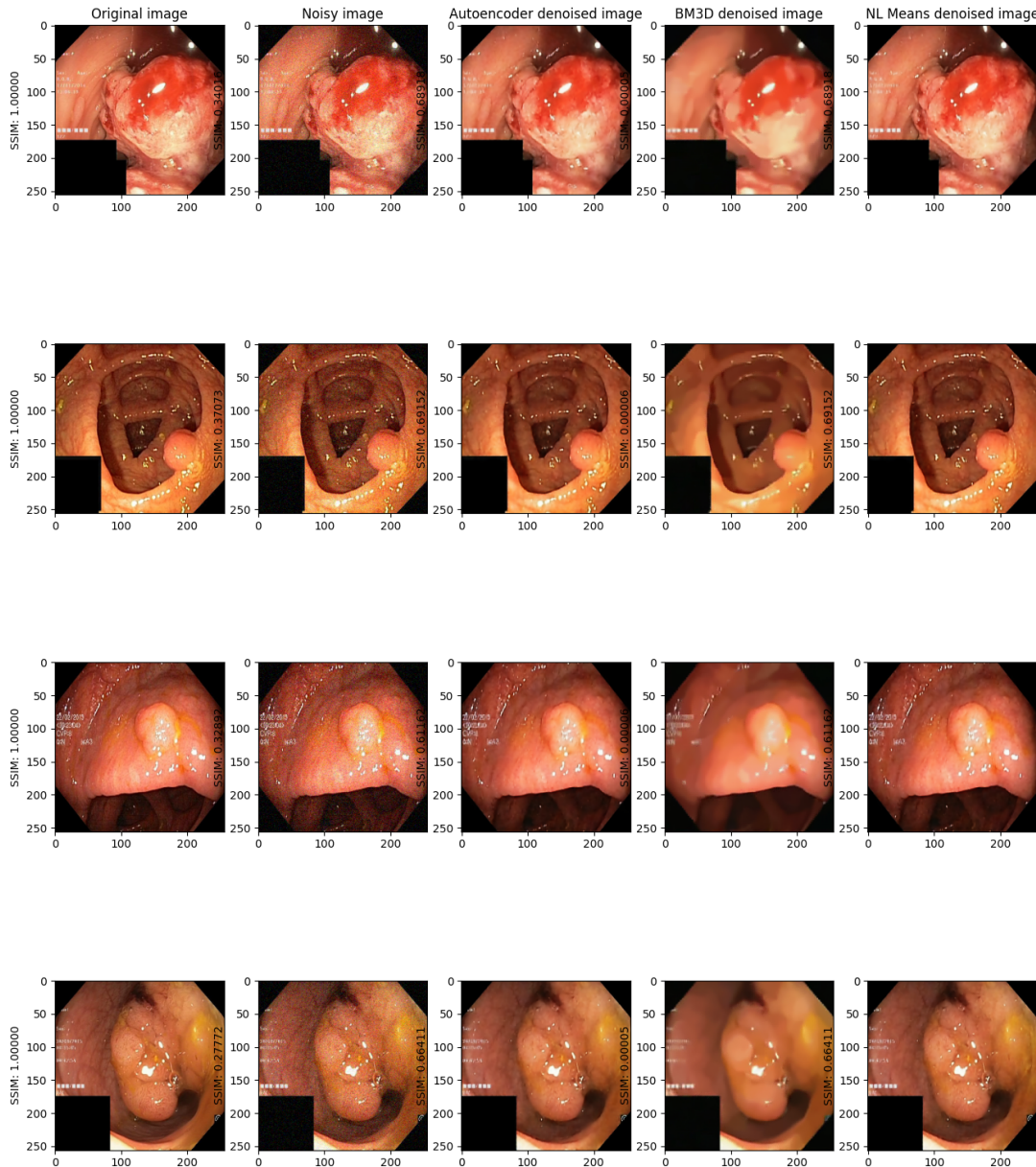


Figure 16: Denoising performance of CAE on different Gaussian noise patterns. Left column shows original images, second column is noisy images with noise levels of $\mu_n = 0$; $\sigma_n = 0.7$; third to fifth row shows denoising results

that, the time consumption is also an important consideration. Because our dataset has a large size. The less time usage is, the more efficient performance is. That is the reason why i also make an experiment to compare the time consumption of these above method. The result is shown in the Table. It is clear to see that CAE out-performs any other method in

	C-BM3D		NL-Mean		CAE	
	Training	Testing	Training	Testing	Training	Testing
Time (s) (for 1 sample)	0	69.62	0	0.2534	550/ 50 epochs	0.0191

time consumption. It is a advantage of Deep Learning in testing/ validating phase.

5 Conclusion

I have shown that denoising autoencoder constructed using convolutional layers can be used for efficient denoising of medical images. In contrary to the belief, I have shown that good denoising performance can be achieved as well as the low time consumption. However, the main disadvantage of deep learning method is that the input has to be in the same resolution. While other method can maintain the original resolution, deep learning has to convert them to a certain one (256×256 in this case). It can make an information loss when we up-scaling the image into the original resolution.

References

- [1] American Cancer Society. “Cancer Statistics, 2021”. In: *CA: a cancer journal for clinicians* (Jan. 2021).
- [2] Mosaburo Kainuma et al. “The association between objective tongue color and endoscopic findings: Results from the Kyushu and Okinawa population study (KOPS)”. In: *BMC complementary and alternative medicine* 15 (Oct. 2015), p. 372. DOI: 10.1186/s12906-015-0904-0.
- [3] M Pennazio. “Capsule endoscopy: Where are we after 6 years of clinical use?” In: *Digestive and liver disease : official journal of the Italian Society of Gastroenterology and the Italian Association for the Study of the Liver* 38 (Jan. 2007), pp. 867–78. DOI: 10.1016/j.dld.2006.09.007.
- [4] Michael Wallace and Ralf Kiesslich. “Advances in Endoscopic Imaging of Colorectal Neoplasia”. In: *Gastroenterology* 138 (June 2010), pp. 2140–50. DOI: 10.1053/j.gastro.2009.12.067.
- [5] Federico Carpi et al. “Magnetically Controllable Gastrointestinal Steering of Video Capsules”. In: *IEEE transactions on bio-medical engineering* 58 (Oct. 2010), pp. 231–4. DOI: 10.1109/TBME.2010.2087332.
- [6] Dobromir Filip et al. “Self-Stabilizing Colonic Capsule Endoscopy: Pilot Study of Acute Canine Models”. In: *IEEE transactions on medical imaging* 30 (July 2011), pp. 2115–25. DOI: 10.1109/TMI.2011.2163165.

- [7] Chisato Hamashima et al. “Mortality reduction from gastric cancer by endoscopic and radiographic screening”. In: *Cancer Science* 106 (Oct. 2015), n/a–n/a. DOI: 10.1111/cas.12829.
- [8] Alfonso Gastelum, Lucely Mata, and Brito la Fuente. “Building a three - dimensional model of the upper gastrointestinal tract for computer simulations of swallowing”. In: *Medical & biological engineering & computing* 54 (July 2015). DOI: 10.1007/s11517-015-1338-z.
- [9] Byungkyu Kim et al. “Design and fabrication of a locomotive mechanism for capsule-type endoscopes using shape memory alloys (SMAs)”. In: *IEEE/ASME Transactions on Mechatronics* 10.1 (2005), pp. 77–86. DOI: 10.1109/TMECH.2004.842222.
- [10] Quyen Chu, Gazi Zibari, and J.F. Gibbs. “Surgical Oncology: A Practical and Comprehensive Approach”. In: (Jan. 2015), pp. 3–678. DOI: 10.1007/978-1-4939-1423-4.
- [11] Niwa Miyahara R, Matsuura T Y, and et al. “Prevalence and prognosis of gastric cancer detected by screening in a large Japanese population: data from a single institute over 30 years”. In: *J Gastroenterol Hepatol* (2007), pp. 1435–1442. DOI: 10.1111/j.1440-1746.2007.04991.x.
- [12] Mouen Khashab et al. “Comprehensive analysis of efficacy and safety of peroral endoscopic myotomy performed by a gastroenterologist in the endoscopy unit: A single-center experience”. In: *Gastrointestinal endoscopy* 83 (July 2015). DOI: 10.1016/j.gie.2015.06.013.
- [13] Scott Owens and Henry Appelman. “Atlas of Esophagus and Stomach Pathology”. In: (Jan. 2014), pp. 117–127. DOI: 10.1007/978-1-4614-8084-6_20.
- [14] Eberlein T., Reid B., and Hawk E. “Report of the stomach/esophageal cancers progress review group”. In: *National Cancer Institute, Bethesda, MD* (2002).
- [15] Roukos DH et al. “Gastric cancer: introduction, pathology, epidemiology”. In: *Gastric Breast Cancer* (2002), pp. 1–3.
- [16] David Callacondo et al. “Erratum to “Primary squamous cell carcinoma of the stomach with paraneoplastic leukocytosis: a case report and review of the literature” [Hum Pathol 40 (2009) 1494–1498]”. In: *Human pathology* 41 (Feb. 2010), p. 307. DOI: 10.1016/j.humpath.2009.12.001.
- [17] Anthony Axon. “Is diagnostic and therapeutic endoscopy currently appropriate?: Suggestions for improvement”. In: *Best practice & research. Clinical gastroenterology* 22 (Feb. 2008), pp. 959–70. DOI: 10.1016/j.bpg.2008.07.003.
- [18] David Hurlstone et al. “Efficacy of high magnification chromoscopic colonoscopy for the diagnosis of neoplasia in flat and depressed lesions of the colorectum: A prospective analysis”. In: *Gut* 53 (Mar. 2004), pp. 284–90. DOI: 10.1136/gut.2003.027623.
- [19] M. Liedlgruber and Andreas Uhl. “A Summary of Research Targeted at Computer-Aided Decision Support in Endoscopy of the Gastrointestinal Tract”. In: (May 2011).
- [20] Douglas Guggenheim and Manish Shah. “Gastric cancer epidemiology and risk factors”. In: *Journal of surgical oncology* 107 (Mar. 2013). DOI: 10.1002/jso.23262.

- [21] Tsutomu Namikawa et al. “Primary gastric small cell carcinoma: Report of a case and review of the literature”. In: *Medical molecular morphology* 38 (Jan. 2006), pp. 256–61. DOI: 10.1007/s00795-005-0293-4.
- [22] Elena Korngold. “GISTS—Gastrointestinal Stromal Tumors”. In: *Journal of Gastrointestinal Cancer* 42 (Sept. 2011), pp. 174–175. DOI: 10.1007/s12029-011-9287-8.
- [23] Prof Rogy and Marius Bünger. “Historical perspective and gastric pathophysiology”. In: *Gastric Cancer: Principles and Practice* (June 2015), pp. 3–22. DOI: 10.1007/978-3-319-15826-6_1.
- [24] Masayuki Kato et al. “Magnifying endoscopy with narrow-band imaging achieves superior accuracy in the differential diagnosis of superficial gastric lesions identified with white-light endoscopy: A prospective study”. In: *Gastrointestinal endoscopy* 72 (Sept. 2010), pp. 523–9. DOI: 10.1016/j.gie.2010.04.041.
- [25] Yark Hazewinkel et al. “Endoscopic features of sessile serrated adenomas: Validation by international experts using high-resolution white-light endoscopy and narrow-band imaging”. In: *Gastrointestinal endoscopy* 77 (Feb. 2013). DOI: 10.1016/j.gie.2012.12.018.
- [26] Dennis Jensen et al. “Doppler Endoscopic Probe as a Guide to Risk Stratification and Definitive Hemostasis of Peptic Ulcer Bleeding”. In: *Gastrointestinal endoscopy* 83 (Aug. 2015). DOI: 10.1016/j.gie.2015.07.012.
- [27] Rami Eliakim. “Wireless capsule video endoscopy: Three years of experience”. In: *World journal of gastroenterology : WJG* 10 (June 2004), pp. 1238–9. DOI: 10.3748/wjg.v10.i9.1238.
- [28] Christoph Schlag et al. “Emergency video capsule endoscopy in patients with acute severe GI bleeding and negative upper endoscopy results”. In: *Gastrointestinal endoscopy* 81 (Nov. 2014). DOI: 10.1016/j.gie.2014.09.035.
- [29] Maria Sotiropoulou. “Angiodysplasia”. In: (Jan. 2017), pp. 51–54. DOI: 10.1007/978-3-319-40560-5_1415.
- [30] George Hanna and Alfred Cuschieri. “Image display technology and image processing”. In: *World journal of surgery* 25 (Dec. 2001), pp. 1419–27.
- [31] Michael Gschwandtner et al. “Experimental study on the impact of endoscope distortion correction on computer-assisted celiac disease diagnosis”. In: (Nov. 2010). DOI: 10.1109/ITAB.2010.5687708.
- [32] Michael Gschwandtner et al. “Experimental study on the impact of endoscope distortion correction on computer-assisted celiac disease diagnosis”. In: (Nov. 2010). DOI: 10.1109/ITAB.2010.5687708.
- [33] M. Liedlgruber, Andreas Uhl, and Andreas Vécsei. “Statistical analysis of the impact of distortion (correction) on an automated classification of celiac disease”. In: *Proc IEEE Int. Conf. Digital Signal Process.* (Aug. 2011), pp. 1–6. DOI: 10.1109/ICDSP.2011.6004900.

- [34] Michael Gschwandtner et al. “Improved Endoscope Distortion Correction does not Necessarily Enhance Mucosa-Classification based Medical Decision Support Systems”. In: *Proceedings of the IEEE International Workshop on Multimedia Signal Processing* (Sept. 2012), pp. 158–163. DOI: 10.1109/MMSP.2012.6343433.
- [35] Jorge Bernal, F. J. Sánchez, and F. Vilariño. “Towards automatic polyp detection with a polyp appearance model”. In: *Pattern Recognit.* 45 (2012), pp. 3166–3182.
- [36] Jorge Bernal et al. “WM-DOVA maps for accurate polyp highlighting in colonoscopy: Validation vs. saliency maps from physicians”. In: *Computerized medical imaging and graphics : the official journal of the Computerized Medical Imaging Society* 43 (2015), pp. 99–111.
- [37] Nima Tajbakhsh, S. Gurudu, and Jianming Liang. “Automated Polyp Detection in Colonoscopy Videos Using Shape and Context Information”. In: *IEEE Transactions on Medical Imaging* 35 (2016), pp. 630–644.
- [38] Sharib Ali et al. “Endoscopy artifact detection (EAD 2019) challenge dataset”. In: *ArXiv* abs/1905.03209 (2019).
- [39] Juan Silva et al. “Toward embedded detection of polyps in WCE images for early diagnosis of colorectal cancer”. In: *International Journal of Computer Assisted Radiology and Surgery* 9 (2013), pp. 283–293.
- [40] A. Koulaouzidis et al. “KID Project: an internet-based digital video atlas of capsule endoscopy for research purposes”. In: *Endoscopy International Open* 5 (2017), E477–E483.
- [41] Y. Guo and B. Matuszewski. “GIANA Polyp Segmentation with Fully Convolutional Dilation Neural Networks”. In: *VISIGRAPP* (2019).
- [42] Jorge Bernal et al. “Polyp Detection Benchmark in Colonoscopy Videos using GTCreator: A Novel Fully Configurable Tool for Easy and Fast Annotation of Image Databases”. In: (2018).
- [43] the gastrointestinal site. “Gastrolab”. In: <http://www.gastrolab.net/index.htm>. Accessed: 2019-12-12 (2019).
- [44] Endoatlas. “Weo clinical endoscopy atlas”. In: <http://www.endoatlas.org/index.php>. Accessed: 2019-12-12 (2019).
- [45] UCI. “Gastrointestinal lesions in regular colonoscopy dataset”. In: (2019). URL: http://www.depeca.uah.es/colonoscopy_dataset/.
- [46] Atlas. “The atlas of gastrointestinal endoscope”. In: (2019). URL: http://www.endoatlas.com/atlas_1.html.
- [47] Atlas. “El salvador atlas of gastrointestinal video endoscopy”. In: (2019). URL: <http://www.gastrointestinalatlas.com/index.html>.
- [48] Konstantin Pogorelov et al. “KVASIR: A Multi-Class Image Dataset for Computer Aided Gastrointestinal Disease Detection”. In: *Proceedings of the 8th ACM on Multimedia Systems Conference* (2017).

- [49] Debesh Jha et al. “Kvasir-SEG: A Segmented Polyp Dataset”. In: *ArXiv* abs/1911.07069 (2020).
- [50] Konstantin Pogorelov et al. “Nerthus: A Bowel Preparation Quality Video Dataset”. In: *Proceedings of the 8th ACM on Multimedia Systems Conference* (2017).
- [51] Bhawna Goyal et al. “Noise Issues Prevailing in Various Types of Medical Images”. In: *Biomedical and Pharmacology Journal* 11 (Sept. 2018), pp. 1227–1237. DOI: 10.13005/bpj/1484.
- [52] N. Obukhova et al. “Review of Noise Reduction Methods and Estimation of their Effectiveness for Medical Endoscopic Images Processing”. In: *2018 22nd Conference of Open Innovations Association (FRUCT)* (2018), pp. 204–210.
- [53] V. Gopi, P. Palanisamy, and S. I. Niwas. “Capsule Endoscopic Colour Image Denoising Using Complex Wavelet Transform”. In: (2012).
- [54] John Immerkær. “Fast Noise Variance Estimation”. In: *Comput. Vis. Image Underst.* 64 (1996), pp. 300–302.
- [55] Pietro Perona and Jitendra Malik. “Scale-Space and Edge Detection Using Anisotropic Diffusion”. In: *IEEE Trans. Pattern Anal. Mach. Intell.* 12 (1990), pp. 629–639.
- [56] L. Rudin and S. Osher. “Total variation based image restoration with free local constraints”. In: *Proceedings of 1st International Conference on Image Processing* 1 (1994), 31–35 vol.1.
- [57] Ö. N. Subakan et al. “Feature Preserving Image Smoothing Using a Continuous Mixture of Tensors”. In: *2007 IEEE 11th International Conference on Computer Vision* (2007), pp. 1–6.
- [58] R. Coifman and D. Donoho. “Translation-Invariant DeNoising”. In: (1995).
- [59] L. Yaroslavsky, K. Egiazarian, and J. Astola. “Transform domain image restoration methods: review, comparison, and interpretation”. In: (2001).
- [60] David Zhang and Zhou Wang. “Image information restoration based on long-range correlation”. In: *IEEE Trans. Circuits Syst. Video Technol.* 12 (2002), pp. 331–341.
- [61] Kostadin Dabov et al. “Image Denoising by Sparse 3-D Transform-Domain Collaborative Filtering”. In: *IEEE Transactions on Image Processing* 16 (2007), pp. 2080–2095.
- [62] Kostadin Dabov et al. “Color Image Denoising via Sparse 3D Collaborative Filtering with Grouping Constraint in Luminance-Chrominance Space”. In: *2007 IEEE International Conference on Image Processing* 1 (2007), pp. I - 313-I –316.
- [63] A. Krizhevsky, Ilya Sutskever, and Geoffrey E. Hinton. “ImageNet classification with deep convolutional neural networks”. In: *Communications of the ACM* 60 (2012), pp. 84–90.
- [64] Geoffrey E. Hinton et al. “Deep Neural Networks for Acoustic Modeling in Speech Recognition: The Shared Views of Four Research Groups”. In: *IEEE Signal Processing Magazine* 29 (2012), pp. 82–97.

- [65] Ilya Sutskever, Oriol Vinyals, and Quoc V. Le. “Sequence to Sequence Learning with Neural Networks”. In: *NIPS* (2014).
- [66] Pascal Vincent et al. “Extracting and composing robust features with denoising autoencoders”. In: *ICML '08* (2008).
- [67] Pascal Vincent et al. “Stacked Denoising Autoencoders: Learning Useful Representations in a Deep Network with a Local Denoising Criterion”. In: *J. Mach. Learn. Res.* 11 (2010), pp. 3371–3408.
- [68] Junyuan Xie, Linli Xu, and Enhong Chen. “Image Denoising and Inpainting with Deep Neural Networks”. In: *NIPS* (2012).
- [69] Harold Christopher Burger, Christian J. Schuler, and S. Harmeling. “Image denoising: Can plain neural networks compete with BM3D?” In: *2012 IEEE Conference on Computer Vision and Pattern Recognition* (2012), pp. 2392–2399.